

Seismic performance of mixed column composed of square CFST column and circular RC column in Chinese archaized buildings

Jiayang Xue^a, Chaofeng Zhou^{*} and Jianpeng Lin^b

College of Civil Engineering, Xi'an University of Architecture and Technology, Xi'an, China

(Received February 11, 2018, Revised September 27, 2018, Accepted October 5, 2018)

Abstract. This paper presents some quasi-static tests for 4 mixed columns composed of CFST column and RC column. The seismic performance and failure mode were studied under low-cyclic revised loading. The failure mode was observed under different axial compression ratios. The hysteretic curve and skeleton curve were obtained. The effects of axial compression ratio on yield mechanism, displacement ductility, energy dissipation, stiffness and strength attenuation were analyzed. The results indicate that the failure behavior of CFST-RC mixed column with archaized style is mainly caused by bending failure and accompanied by some shear failure. The axial compression ratio performs a control function on the yielding order of the upper and lower columns. The yielding mechanism has a great influence on the ductility and energy dissipation capacity of specimens. Based on the experiment, finite element analysis was made to further research the seismic performance by ABAQUS software. The variable parameters were stiffness ratio of upper and lower columns, axial compression ratio, yielding strength of steel tube, concrete strength and rebar ratio. The simulation results show that with the increase of stiffness ratio of the upper and lower columns, the bearing capacity and ductility of specimens can correspondingly increase. As the axial compression ratio increases, the ductility of the specimen decreases gradually. The other three parameters both have positive effect on the bearing capacity but have negative effect on the ductility. The results can provide reference for the design and engineering application of mixed column consisted of CFST-RC in Chinese archaized buildings.

Keywords: mixed column composed of CFST-RC; archaized buildings; experimental research; seismic performance; finite element analysis

1. Introduction

Chinese ancient architectures are the crystallization of the long historical culture of Chinese nation, with high historical value and scientific value. Most of Chinese ancient architectures are made of wood, but also have unique style and connection. Many researches indicate that the timber structure can show perfect seismic performance through the energy dissipation of column base and mortise-tenon (Darvishi *et al.* 2016, Eckelman and Haviarova 2015). As time goes on, due to the natural disasters and human factors such as the war, most of the ancient buildings have been seriously destroyed. Only a few ancient wooden structures have been preserved in China, such as Yingxian Wooden Pagoda and Forbidden City.

In order to inherit the precious cultural heritage, the thought of archaized building constructed with modern construction materials are put forward. The archaized building, which combines modern materials and construction techniques with ancient architecture culture connotation, is a new type of architecture form (Wang 2012). Archaized building is the perfect combination of

traditional construction law and modern construction material. It not only enhances the ability and durability of the structure against disasters, but also inherits the characteristics of the ancient architecture such as graceful appearance and magnificent style. What's more, Chinese civilization is inherited and carried forward by the archaized building (Gong 2015, Xue *et al.* 2015). Therefore, a large number of archaized buildings have been built in recent years, as shown in Fig. 1.

Many researches indicate that the composite structure or the hybrid structure, especially the steel and concrete composite structure, has good seismic performance, reasonable cost and good fire resistance, but also can effectively control the sectional size of the component (Chacón *et al.* 2013, Chitawadagi *et al.* 2012, Ekmekyapar and Al-Eliwi 2016, Han and An 2014, Hajjar 2015, Ouyang and Kwan 2018, Portolés *et al.* 2011, Sundararaja and Prabhu 2013, Skalomenos *et al.* 2015, Yadav *et al.* 2016, Patel *et al.* 2016). Therefore, the composite structure and the hybrid structure have a good application prospect in archaized buildings. For the ancient buildings, circle column is usually used and the Dou-Gong is placed at the column top. However, in order to ensure the continuity of vertical force transmission and the convenience of installing the Dou-Gong for antique buildings, a rectangular cross-section shrunken column needs to be set on the top of the circle column, thus forming an archaized mixed column. The CFST column is chosen as the upper column, which

*Corresponding author, Ph.D. Candidate,

E-mail: zhouchaofeng163@163.com

^a Professor, Ph.D., E-mail: jiayang_xue@163.com

^b M.E., E-mail: 445168577@qq.com



(a) Shaanxi History Museum



(b) Famen Temple

Fig. 1 Archaized buildings

has a high bearing capacity and stiffness because of the confining effect of steel tube. RC column is taken as the lower column. The mixed column consists of CFST and RC, which is not exactly the same as the modern transfer column. The vertical stiffness and cross-section of mixed column in archaized buildings varies widely along the column height.

As the mixed column presented in the paper is special in the shape and mechanical properties, lots of references about CFST column and transfer column are browsed before studying the mixed column composited of RC column and CFST column. Zhao and Shao (2010) conducted an experimental study for one reinforced column and eight SRC-RC transfer columns with different constructional measures under low cyclic reversed loading. Based on the experiment, the influence of the different constructional measures on seismic behavior of SRC-RC transfer columns was discussed. Wu *et al.* (2016) carried out some experiments for 16 transfer columns and 1 reinforced concrete column under low cyclic reversed loading. The test results showed three failure modes for columns, including shear failure, bond failure and bend failure. Additionally, all transfer columns showed similar discipline of stiffness degradation and better energy dissipation capacity. Suzuki *et al.* (2000) conducted some low-cycle cyclic loading experiments for four half-span ratio short columns with a ratio of shear to span of 1.5. The experiment mainly studied the influence of the extension height of the middle column of transitional column on the mechanical behavior of the column. Prabhu *et al.* (2015) presented the feasibility analysis on the application of CFRP composite strips to strengthen the CFST column member under axial loading. The experimental results revealed that bonding of CFRP composites effectively

delayed the local buckling of the columns and also reduced the axial deformation by providing a confinement/restraining effect against the elastic deformation at both spacing. Han and An (2014) carried out a finite element analysis on the behavior of the composite columns and put forward a simplified formulas for predicting its ultimate strength.

As a mixed column simplified from archaized buildings, there are few researches on the seismic performance of mixed column consist of CFST and RC column. The large difference between archaized buildings and modern buildings results in the great change of the force performance of their structural components, and the existing norms are no longer fully applicable to the structure design of archaized buildings. Therefore, this paper presents some experiments for 4 mixed columns composited of CFST and RC under the low cyclic reversed loading and parameter analysis in order to research the seismic performance of this kind of mixed column with archaized style. The seismic performance and yielding mechanism with different design parameters are discussed. This study attempts to help providing some design methods and suggestions of the archaized building.

2. Test program

2.1 Specimen design and production

The prototype was taken from the eaves of the main hall of the Buddhist college of Famen Temple (the upper part was a square CFST column and the lower part was a circular RC column), as shown in Fig. 2. According to the different design index in slenderness ratios of the upper

Table 1 Test parameters of specimens

Specimen type	Specimen ID	Steel tube (mm)	n	λ	Shear bolt (mm)	Number of bolt	$\rho_s/\%$	$\rho_v/\%$
A	LJ-1	□180×180×8	0.25	61.35	19×80	28	1.13%	0.68%
	LJ-2	□180×180×8	0.5	61.35	19×80	28	1.13%	0.68%
B	LJ-3	□250×250×10	0.25	83.14	19×80	40	0.80%	0.55%
	LJ-4	□250×250×10	0.5	83.14	19×80	40	0.80%	0.55%

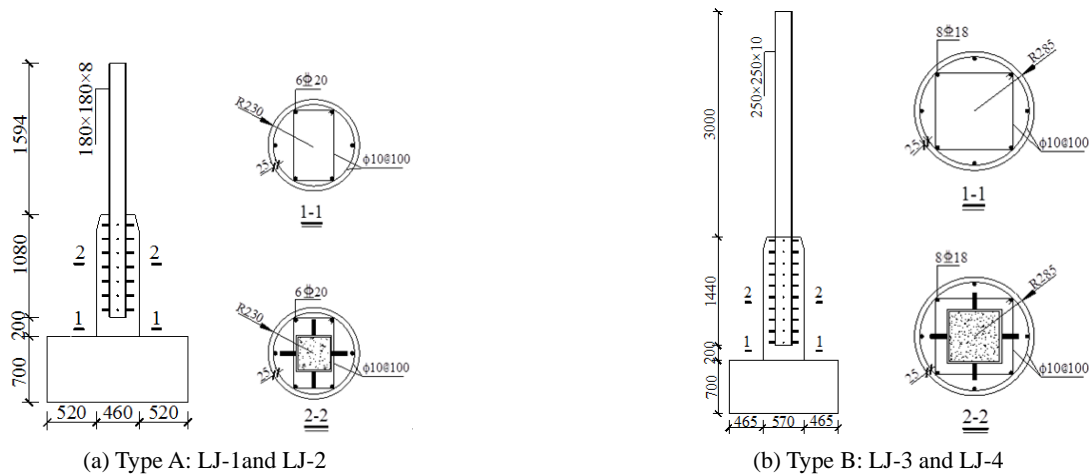


Fig. 2 Dimension of specimens

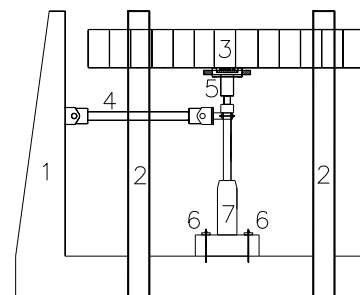
CFST columns, the anchorage length of the steel tube and the reinforcement ratio, four variable cross-section specimens were designed and divided into two types: A and B. In order to study the seismic performance of the upper and lower column connecting transition zone, the main parameters of the design were the axial compression ratios of CFST columns. The detail dimensions of the specimen are shown in Fig. 2. The specific test parameters are shown in Table 1, where n is the axial compression ratio, λ is the slenderness ratio, ρ_s is the longitudinal reinforcement ratio in the column cross section, ρ_v is the stirrup ratio in the column cross section.

To ensure the anchoring effect of the upper square steel tube and the lower RC columns, the square steel tube wrapped in concrete were welded with shear bolts. The distance of shear bolts is 150 mm. The bottom of the tube is 200 mm distant from the top of the base. The specimens were poured with C30 micro concrete of which the maximum aggregate size was about 10 mm. The base and the concrete inside the steel tube were first poured, and then the RC circular column was poured after the steel tube was positioned by the theodolite. The measured values of cube compressive strength of CFST column and RC column were 35.46 MPa, 40.57 MPa respectively. The material properties of steel are shown in Table 2.

2.2 Loading program and measuring points layout

The loading device is shown in Fig. 3. The vertical load was applied by the hydraulic jack, and the horizontal

repetitive load was applied by the MTS hydraulic servo actuator. During the test, the vertical load was applied to the design axial pressure ratio through the hydraulic jack, and then the horizontal load was applied by the force-displacement mixed control method. Before the yielding of the specimen, the force control was used with each stage load of one cycle and the load application differential of 5 kN~10 kN. After the yielding, the displacement control was taken. Each displacement-loading step was cycled three times with the multiple of the yielding displacement until



1 reaction wall. 2 reaction steel frame. 3 reaction girder. 4 MTS electro-hydraulic servo actuator. 5 hydraulic jack. 6 compression beams. 7 specimen

(a) Schematic diagram of loading device



(b) Actual loading device

Table 2 Mechanical parameters of steel and reinforced bar

Steel	f_y / MPa	f_u / MPa	E_s / 10^5 MPa	$\epsilon_y/10^{-6}$
φ10	317.2	517.5	2.32	1367
φ18	446.0	623.6	1.98	2252
φ20	431.6	625.0	2.01	2147
□180×180×8	323.8	450.2	1.91	1700
□250×250×10	259.9	372.8	1.94	1340

Fig. 3 Test setup

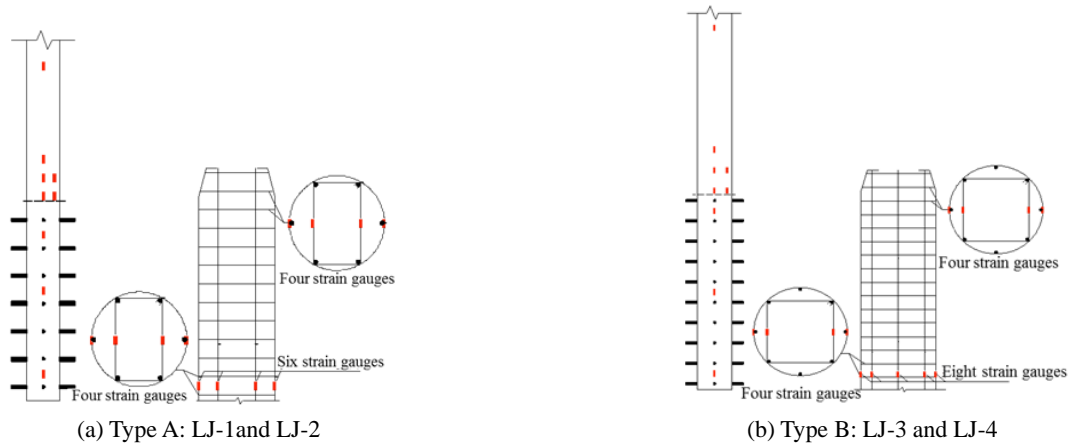


Fig. 4 Arrangement of strain gauges

the load falls to 85% of the maximum load or the loading ends when the specimen is damaged.

In order to study the stress of the roots and the connecting areas of the upper and lower columns, the strain gauges are arranged on the corresponding steel pipes and steel bars respectively. The strain gauges are arranged as shown in Fig. 4. Five displacement gauges are arranged along the scape of the upper and lower columns to measure the flexural deformation of the specimen and the displacement meter is arranged as shown in Fig. 3(b).

3. Experimental results and analyses

3.1 Analysis on failure mode

At the end of the loading, the ultimate failure mode of specimens was mainly bending failure, with some shear failure characteristics. There were some plastic hinges at the root of CFST column and RC column. At the beginning of loading, many horizontal cracks successively appeared in the middle and lower part of the RC column. The concrete cracks at the variable cross-section of the specimen extended from the corner of steel tube to the outside of the column and developed downward along the scape to form vertical cracks which divided concrete at the top of RC column into four parts. With the increase of the load, the strain data at the root of CFST and RC column grew dramatically, and then the steel tube and the longitudinal reinforcement yielded successively. Meanwhile, no more new horizontal cracks appeared. In the displacement control stage, with the increase of displacement, the CFST column gradually entered into the yielding stage. The CFST column in anchoring section continuously squeezed the RC column, which resulted in that the shear bearing capacity of the stirrups in the anchoring section is weakened. With the increase of the loading, the stirrups can't withstand the shear capacity. Therefore, more oblique cracks appear in the anchoring section of CFST column. The original horizontal cracks developed to the north and south side (parallel to the actuator), then began to extend downward obliquely where the concrete at column base began to peel off. As the control displacement continued to increase, a small amount

of concrete crushed off at the column base, and the longitudinal rebar exposed. When the horizontal bearing capacity dropped to 85% of the peak, the experiment was stopped. The failure mode of the specimen is shown in Fig. 5.

3.2 Analysis on yielding mechanism

For specimens LJ-2 and LJ-4, when the control displacement reached 40 mm, the strains at the root of CFST were up to 2000×10^{-6} , while the strains of longi-

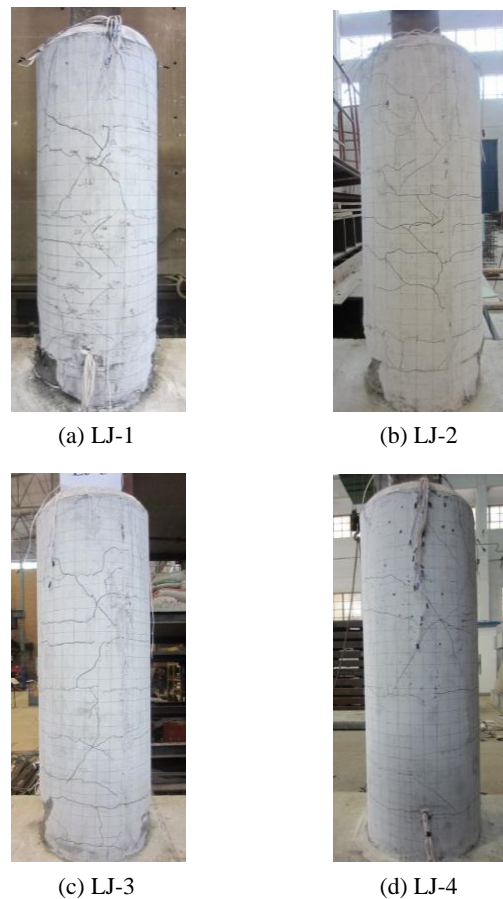


Fig. 5 Failure mode of specimens

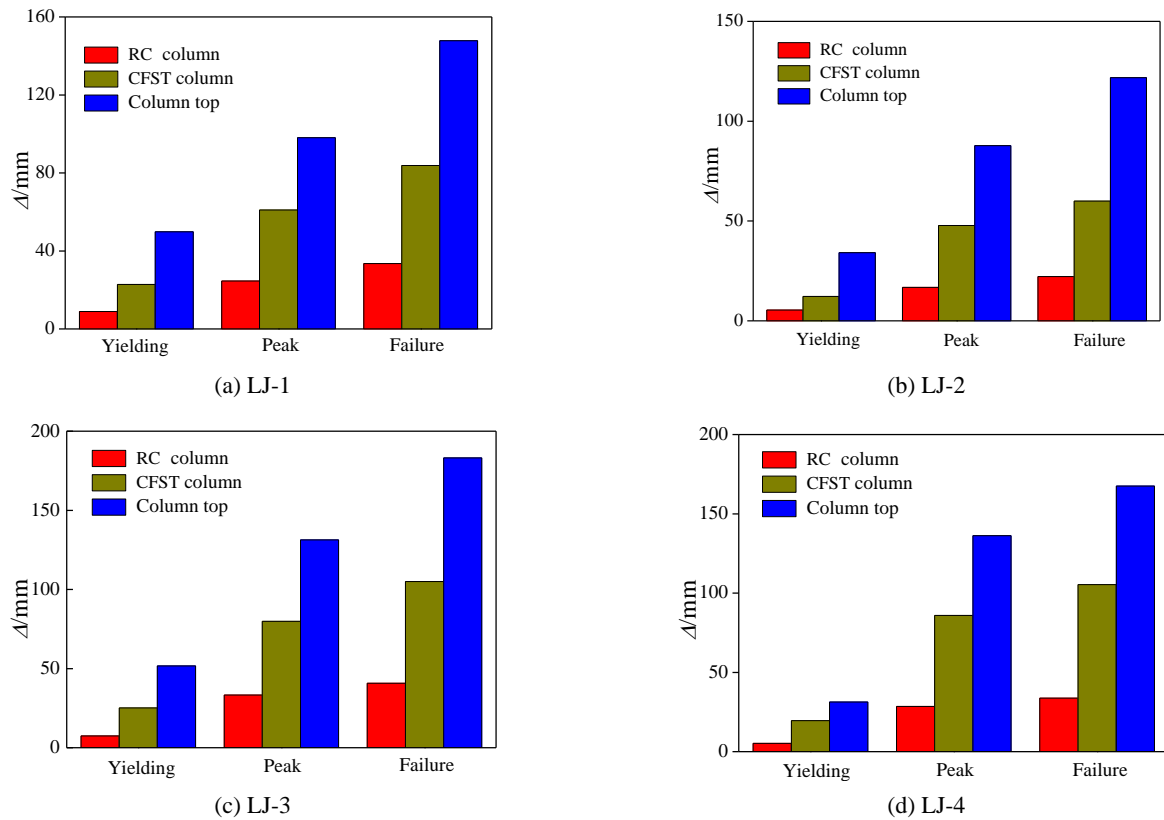


Fig. 6 Displacement distribution of CFST-RC column

tudinal rebar were still about 800×10^{-6} . According to the strain data, it could be seen that the strains of steel tube grew rapidly while that of longitudinal rebar increased slowly. The steel tube reached yielding prior to the longitudinal rebar during the loading process. For specimens LJ-1 and LJ-3, when the force reached 50 kN, some strains of longitudinal rebar exceeded 2500×10^{-6} , which indicated that the longitudinal rebar entered into the yielding stage. The longitudinal rebar reached yielding prior to the steel tube. By analyzing the test results, the axial compression ratio was considered as an important role in controlling the yielding order of CFST column and RC column. Because the RC column had a higher sectional flexural stiffness than the CFST column while the slenderness of the CFST column was much larger than that of the RC column, which made the lateral ability of upper CFST column much smaller than that of the lower RC column. The lateral deformation of the upper and lower columns was not coordinated. When the axial compression ratio of the specimen was relatively large, the lateral stiffness of RC column was large under the horizontal load with the small lateral displacement. However, the lateral displacement of CFST column accounted for the majority of overall displacement, which aggravated the $P-\Delta$ effect and then produced a larger additional bending moment at the root of the CFST column. Therefore, the steel tube at the root of CFST column entered into the yielding stage first. Otherwise, when the axial compression ratio was relatively small, the lateral displacement of the RC column increased under the horizontal load, and the lateral displacement of the CFST column accounted for a smaller proportion in the

overall lateral displacement. The overall co-deformation ability of the specimen was better with smaller influence of the $P-\Delta$ effect, and the longitudinal bars of the RC column yielded first.

3.3 Lateral displacement analysis

The CFST-RC column has a stiffness change at the variable cross section, and the upper and lower columns have great difference in the lateral resistance. The displacement of the CFST column and the RC column is shown in Fig. 6. Table 3 shows the relative displacement of the CFST column, the RC column and the displacement of the column top.

It can be seen from Fig. 6 and Table 3 that when the CFST-RC column reaches the yielding point, compared with the specimen of $n = 0.25$, the vertex displacements of the LJ-2 and LJ-4 specimens with $n = 0.50$ respectively reduce by 33.96% and 17.18%, their displacements of CFST column respectively decrease by 31.83% and 14.35%, and the displacements of RC column respectively decrease by 31.83% and 14.35%. It can be seen that with the increase of axial compression ratio, each part displacement gets reduced. When the horizontal loading reaches the peak point, compared with the specimen of $n = 0.25$, the vertex displacement, CFST column displacement and RC column displacement of the LJ-2 with $n = 0.50$ respectively decrease by 28.43%, 21.63% and 46.61%. While the vertex displacement and CFST column displacement of the LJ-4 with $n = 0.50$ increase by 0.38% and 7.53% respectively, the displacement of RC column

Table 3 Displacement of characteristic points

Specimen	Top displacement /mm			Top displacement of CFST column /mm			Top displacement of RC column /mm		
	Yielding	Peak	Failure	Yielding	Peak	Failure	Yielding	Peak	Failure
LJ-1	33.54	83.82	147.84	24.57	60.99	98.04	8.97	22.83	49.80
LJ-2	22.15	59.99	121.84	16.75	47.80	87.71	5.40	12.19	34.13
LJ-3	40.75	104.99	183.07	33.31	79.85	131.34	7.44	25.14	51.73
LJ-4	33.75	105.39	167.53	28.53	85.86	136.24	5.22	19.53	31.29

decreases by 22.32%, indicating that the displacement of the RC column gradually decreases with the increase of the axial compression ratio. This phenomenon is particularly evident in Type B specimens, which indicates that the root of CFST column with the larger axial compression ratio is easy to be damaged. RC column has less damage. The larger axial compression ratio aggravates the incongruity of the CFST column and the RC column displacement.

3.4 Hysteretic curve and skeleton curve

The main test results of the CFST-RC column in the antique buildings are shown in Table 4, where P_{cr} , P_y , P_m and P_u respectively stand for the cracking load, yielding load, peak load and failure load, Δ_{cr} , Δ_y , Δ_m and Δ_u are the corresponding displacement respectively. The ductility coefficient μ takes the ratio of Δ_u to Δ_y . The hysteretic curves and the skeleton curves are shown in Figs. 7 and 8, respectively.

(1) At the initial stage of loading, the specimens are all in the elastic stage. The curves of load-displacement

basically vary linearly with small area, which indicates that the dissipated energy is little by deformation. With the increase of the horizontal load, the concrete gradually cracks. Meanwhile, the plastic deformation increases and the lateral stiffness of the specimen start to degenerate. The hysteretic curve gradually leans to the displacement axis, and the enclosed area gradually increases.

- (2) After the yielding, with the increase of the displacement, the plastic deformation develops rapidly. The hysteretic curves become plump, which indicates that more energy is dissipated. The stiffness degenerates more severely. With the increase of the cycle times, the damage accumulation of the column gradually intensifies and the intensity continuously degrades.
- (3) The hysteretic curves of the LJ-1 and LJ-3 are relatively plump, with a slight "pinch" phenomenon. The LJ-1 and LJ-3 have better deformability under the action of small axial compression ratio ($n = 0.25$). Under the influence of the yielding

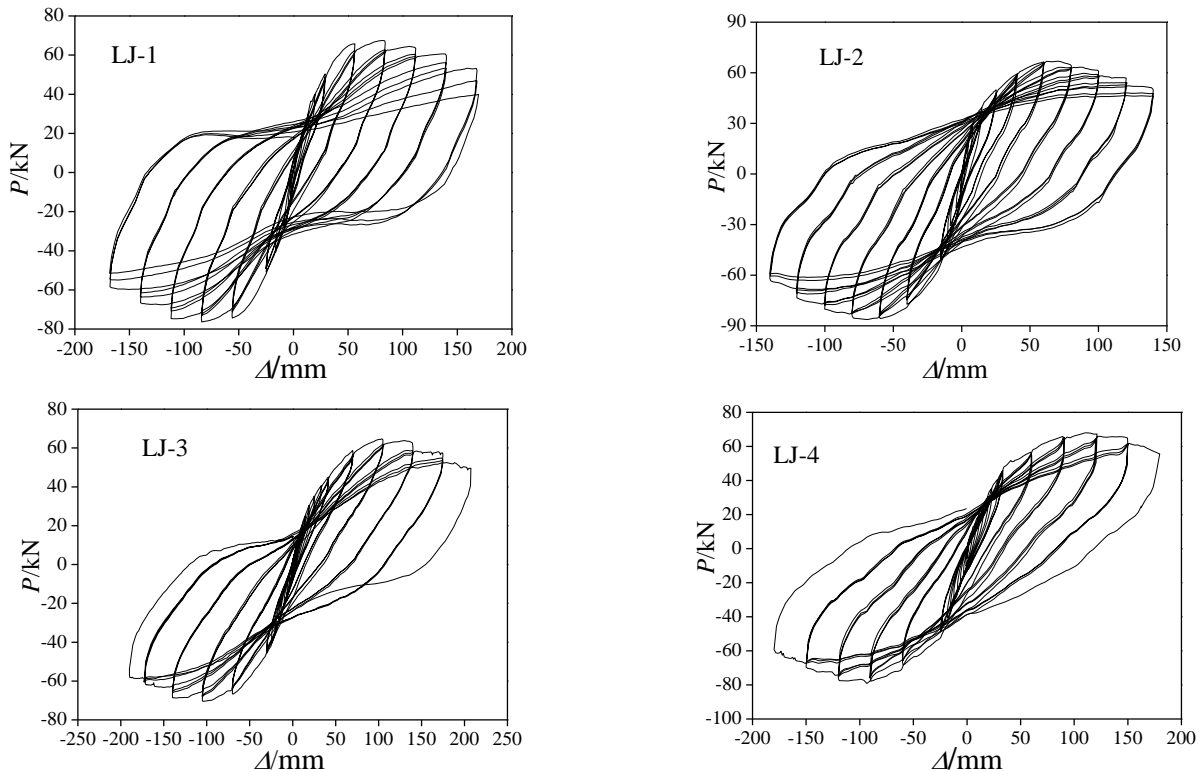


Fig. 7 Hysteretic curves of specimens

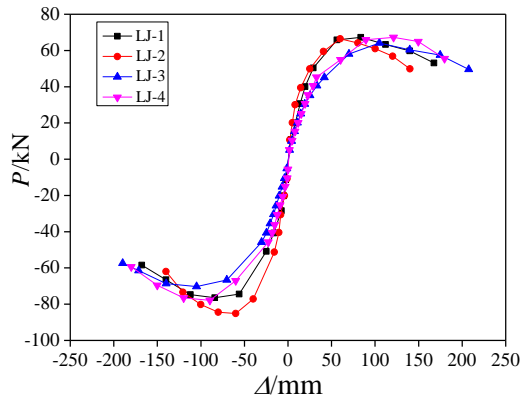


Fig. 8 Skeleton curves of specimens

mechanism, the longitudinal bar of the RC column firstly yields. The oblique cracks on the surface of RC column fully develop, and the concrete damage in the column base is more serious. However, the hysteretic curves of the LJ-1 and LJ-3 still remain a rather full arched shape due to the configuration of the steel tube.

- (4) The hysteretic curves of the LJ-2 and LJ-4 present full spindles. The reason is that the CFST columns of LJ-2 and LJ-4 specimens first yield at the large axial compression ratio ($n = 0.5$) followed by the longitudinal bars of the RC columns. The concrete of RC column destroys lightly and the good hysteretic behavior of the CFST column is fully exerted. The overall plastic deformation capacity of the specimen is strong without the “Pinch” phenomenon in the hysteretic curve.
- (5) With the increase of the axial compression ratio, the elastic stiffness and horizontal bearing capacity of the specimen slightly increase. In the later stage of loading, the uncoordinated deformation of the CFST and RC columns is aggravated under the larger axial compression ratio. The CFST column has large deformation, which results in that the weak part is formed at the CFST column base. After the peak load, the bearing capacity descends more rapidly.

3.5 Ductility and energy dissipation

The displacement ductility coefficient of each specimen is shown in Table 4, where μ represents the ductility coefficient. It can be seen that the μ of the specimens are all greater than 4, indicating that the CFST-RC column has good ductility. For LJ-2 and LJ-4, the CFST column enters into the yielding stage first followed by the RC column. The displacement of CFST column accounts for a large proportion of the overall displacement of the specimen. The excellent deformation capacity of CFST column is fully exerted. Thus, as shown in Table 4, the displacement ductility coefficients of the LJ-2 and LJ-4 are slightly larger than those of LJ-1 and LJ-3. Meanwhile, the CFST column is used as the upper column, which can make it possible for the column to have better ductility under the large axial compression ratio. Under $n = 0.25$, the specimen LJ-1 and LJ-3 have little difference in terms of displacement ductility coefficients. As the axial compression ratio is 0.5, the ductility coefficient of the LJ-2 is obviously larger than that of the LJ-4. The above phenomenon shows that under the larger axial compression ratio, for the specimen LJ-4 with larger slenderness, the additional bending moment generated from $P-\Delta$ effect will accelerate the damage of the specimen. Therefore, in order to make sure that the good seismic performance of this type of components under the earthquake, the interaction between axial compression ratio and slenderness ratio should be taken into account.

Table 5 shows the equivalent viscous damping coefficient of the specimen in each stage, where h_e represents the coefficient. It can be seen that the energy dissipated by the specimen also gradually increases with the

Table 4 Experimental results

Specimen		LJ-1		LJ-2		LJ-3		LJ-4	
		Positive	Negative	Positive	Negative	Positive	Negative	Positive	Negative
Crack	P_{cr}/kN	19.89	-20.17	30.06	-30.59	30.48	-30.42	35.49	-36.22
	Δ_{cr}/mm	8.01	-4.9	8.1	-8.38	19.14	-16.57	22.97	-15.18
Yielding	P_y/kN	52.25	-58.2	45.08	-60.29	44.26	-51.43	46.41	-50.57
	Δ_y/mm	32.31	-34.77	20.18	-24.12	40.16	-41.34	35.29	-32.2
Peak	P_m/kN	67.31	-76.41	66.45	-85.11	64.17	-70.27	67.26	-77.82
	Δ_m/mm	83.67	-83.97	59.98	-60	105	-104.99	121.18	-89.6
Failure	P_u/kN	57.21	-64.95	56.49	-72.34	54.54	-59.73	57.17	-66.15
	Δ_u/mm	150.59	-145.08	121.35	-122.33	186.9	-179.24	174.88	-160.17
Ductility coefficient	μ	4.42		5.54		4.94		4.96	

Table 5 Equivalent viscous damping coefficient h_e

Specimen	h_e		
	Yielding	Peak	Failure
LJ-1	0.093	0.183	0.281
LJ-2	0.115	0.177	0.306
LJ-3	0.070	0.140	0.233
LJ-4	0.101	0.202	0.311

increase of the load. The calculated h_e of every specimen in the failure stage is greater than 0.2, indicating that the specimens have good energy dissipation capacity. In the same stage, the h_e of the LJ-2 is slightly larger than that of the LJ-1. Under the high axial compression ratio, the steel tube of the specimen enters into the yielding state prior to the longitudinal bar, which results in that more energy is dissipated for LJ-4 in the displacement-control stage. Therefore, the value h_e of LJ-4 is much larger than that of LJ-3. Under the same axial compression ratio, there is no obvious difference in energy dissipation capacity. Under the axial compression ratio of 0.5, the steel tubes of specimens enter into the yield state first and the yielding displacement of steel tube in type B specimen is larger than that of steel tube in type A specimen. So the energy dissipation capacity of type B specimen is slightly stronger than that of type A specimen in the peak stage and failure stage.

3.6 Stiffness and strength degradation

Fig. 9 shows the rule of the stiffness degradation. It can be seen from the curves that the stiffness degradation rate of the specimens with different axial compression ratios is basically the same with the increase of the displacement. However, in the displacement-control stage, the stiffness of the specimen with the axial compression ratio of 0.5 is greater than that of the specimen with the axial compression ratio of 0.25. The reason is that the overall displacement with axial compression ratio of 0.5 is smaller than that under with axial compression ratio of 0.25. The lateral displacement of RC column with axial compression ratio of

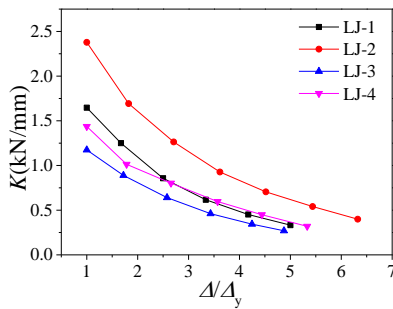


Fig. 9 Stiffness degradation curves of specimen

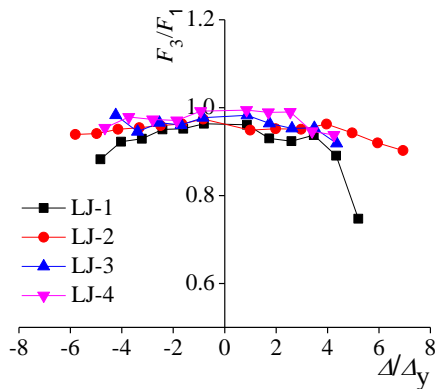


Fig. 10 Strength degradation curves

0.5 is smaller than that with axial compression ratio of 0.25, which results in that the specimens LJ-2 and LJ-4 still maintain a high lateral stiffness in the test.

Fig. 10 shows the curve of the strength degradation, where F_1 and F_3 respectively represent the horizontal bearing capacity of the first and third cycles of the same displacement, F_3/F_1 represents the degree of strength attenuation in the three-cycle displacement. It can be seen from the Fig. 10 that with the increase of the displacement and cycle times, the strength of the specimens decays rapidly. The phenomenon indicates that the concrete damages seriously. In addition to LJ-1, the strength degradation of the remaining specimens is not obvious and their horizontal bearing capacities can reach above 90% of the capacity in the first-cycle, indicating that the specimens maintain a high later bearing capacity under the repeated load. The strength degradation of specimens with $n = 0.25$ is slightly worse than that of specimens with $n = 0.5$. The axial compression ratio has an effect on the yielding mechanism. For LJ-3 and LJ-1 with $n = 0.25$, the RC column damages seriously and the strength decreases rapidly under the influence of yielding mechanism. For LJ-4 and LJ-2 with $n = 0.5$, the CFST columns firstly yield. Due to the constraint of the steel tube, the concrete filled in steel tube still has high bearing capacity. Therefore, the CFST column can maintain high bearing capacity.

4. Finite element analysis

ABAQUS software is adopted for the static elastic-plastic analysis of the CFST-RC column in antique buildings (Wang and Chen 2006).

4.1 Constitutive model of material

4.1.1 Concrete constitutive model

The concrete constitutive model presented in Chinese Code for Design of Concrete Structures (GB 50010-2010) is adopted for concrete of RC column as shown in Fig. 11. The parameters in Fig. 11 are listed in Table 6, where the symbol meaning can be found in the [Nomenclature]. The confined concrete constitutive model proposed by Liu (2006) is adopted when the concrete of CFST column is in compression. The constraining factor can be calculated according to Eq. (1), where ζ is equal to 2.46 for Type-A

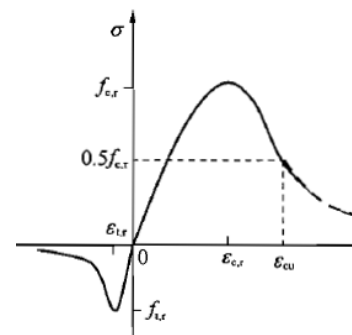


Fig. 11 Stress-strain curve of concrete in RC column

Table 6 Parameters of concrete in RC column

Concrete		RC
Tension	$f_{t,s}$ (N/mm ²)	3.03
	$\varepsilon_{t,r}$ (10 ⁻⁶)	118
	α_t	2.82
Compression	$f_{c,r}$ (N/mm ²)	30.83
	$\varepsilon_{c,r}$ (10 ⁻⁶)	1653
	α_c	1.41
	$\varepsilon_{c,u}$ (10 ⁻⁶)	3747

specimen and ζ is equal to 1.75 for Type-B specimen. When the concrete of CFST column is in tension, the stress-strain curve proposed by Shen *et al.* (1993) is used to simulate the mechanical property of concrete.

$$\zeta = \frac{A_s f_y}{A_c f_{ck}} \quad (1)$$

where A_s represents the area of steel tube; f_y represents the yielding strength of steel; A_c represents the area of concrete section; f_{ck} represents the standard axial compression strength of concrete.

4.1.2 Steel constitutive model

The double-linear elastic hardening model is used for the steel as shown in Fig. 12, where E_s and f_y are shown in Table 2, and the hardening coefficient is chosen as 0.01.

4.2 Finite element model

The element C3D8R is used to simulate the concrete and steel tube. The element T3D2 is used for the longitudinal

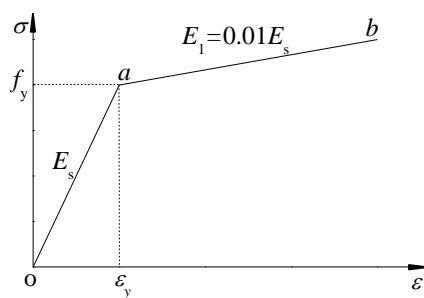


Fig. 12 Stress-strain curve of steel

reinforcement. The bond stress and bond slip between the steel tube and concrete was simulated by the surface contact element. The “hard” contact is adopted for normal action and the defined friction “0.2” is adopted for tangential action (Ghannam *et al.* 2004). The shear bolt on the surface of the square steel tube effectively ensure the co-operation between concrete and steel tube, so the binding constraint is used to define the contact among them. The steel skeleton is considered to be embedded into the concrete. Two analysis steps are set up in the finite element analysis, where the first step is to exert vertical load and the second step is to exert the horizontal displacement. Fig. 13 shows the finite element model.

4.3 Validation of finite element model

The comparison results of skeleton curves are shown in Fig. 14. It indicates that the positive influence of high axial compression ratio on initial stiffness and bearing capacity are not perfectly shown in the numerical calculation. However, as the load increases, the concrete continuously withdraws from work and then the specimens enter into the plastic stage. The difference between calculated results and test results gradually decreases after the yielding point. Overall, the simulation results are accurate and can be used to analyze the mechanical properties of CFST-RC mixed columns.

4.4 Parameter analysis

To further study the seismic performance of the CFST-RC mixed column in archaized buildings, the seismic behaviors under different parameters are analyzed by the finite element analysis. In this paper, the stiffness ratio β of the upper and lower column ($\beta = i_{CFST}/i_{RC}$), the axial compression ratio n , the yielding strength of steel tube f_y , the concrete strength $f_{cu,k}$ and the longitudinal rebar ratio ρ_s are chosen as the main parameters to conduct the analysis. Based on the finite element analysis, the ductility indexes under different parameters are calculated and showed in Table 7.

4.4.1 Stiffness ratio β of the upper to lower column

In order to study the influence of β on the mechanical properties of the specimens, different stiffness ratios β are chosen. For type A specimens, the values are chosen as 0.015, 0.036, 0.075 (test value) and 0.169, respectively. For type B specimens, the values are 0.019, 0.037, 0.113 (test value) and 0.175, respectively.

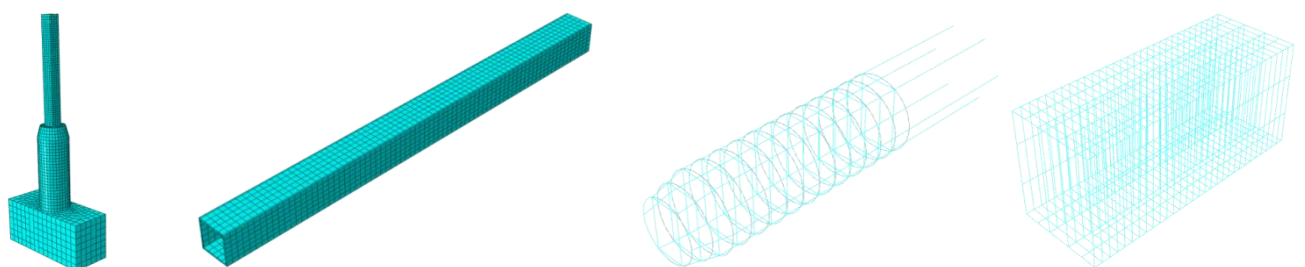


Fig. 13 Finite element model

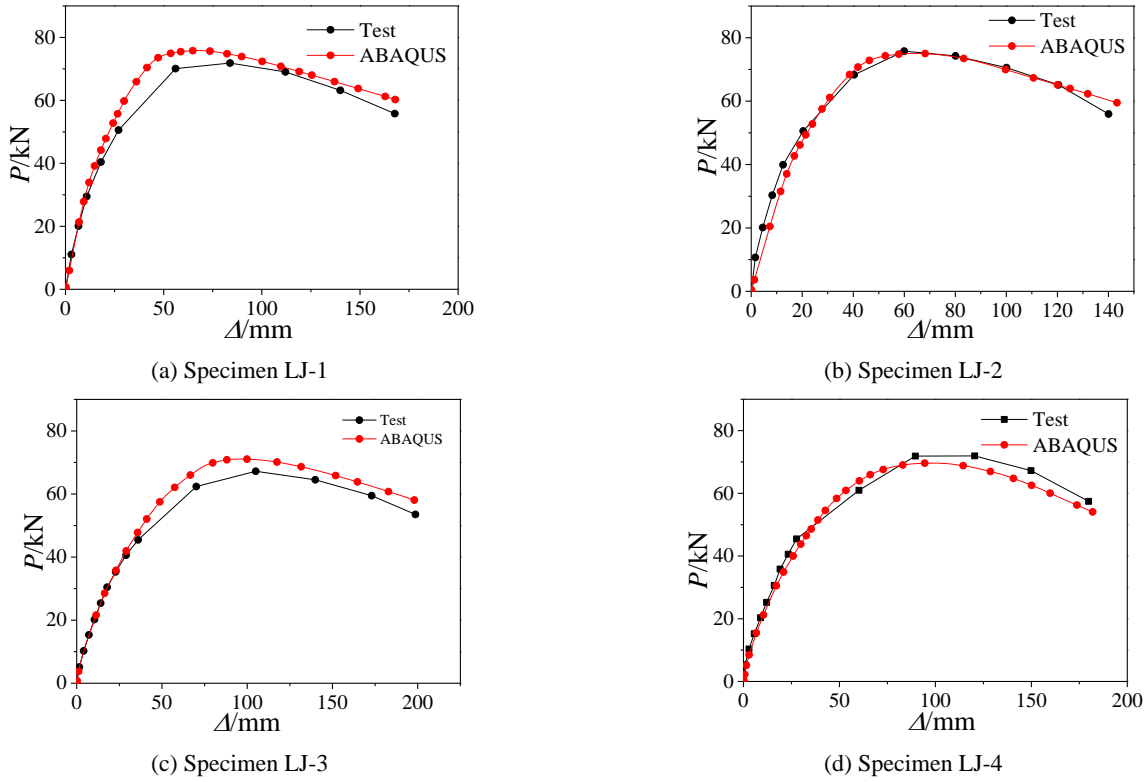


Fig. 14 Comparison of skeleton curves

Table 7 The influence of different parameters on ductility

Specimen	β	μ	n	μ	f_y/MPa	μ	$f_{cu,k}/\text{MPa}$	μ	$\rho_s/\%$	μ
Type A	0.015	2.58	0.15	5.12	235	4.98	30	4.68	0.73	5.57
	0.036	3.66	0.25	4.84	345	4.28	40	4.41	1.13	4.84
	0.075	4.84	0.5	4.38	390	4.18	50	4.20	1.77	4.35
	0.169	4.55	0.75	3.94	420	4.18	60	4.10	2.22	4.34
Type B	0.019	2.03	0.15	4.19	235	3.62	30	3.68	0.80	4.02
	0.037	2.47	0.25	4.02	345	3.03	40	3.63	1.19	3.82
	0.113	4.02	0.5	3.63	390	2.92	50	3.63	1.93	3.76
	0.175	4.44	0.75	3.29	420	2.91	60	3.47	2.50	3.74

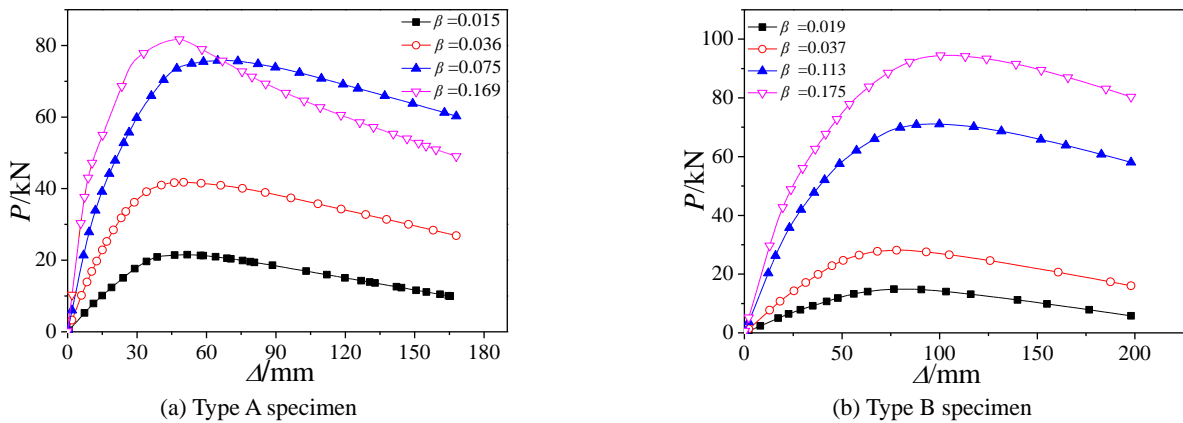


Fig. 15 $P-\Delta$ curve under different stiffness ratios

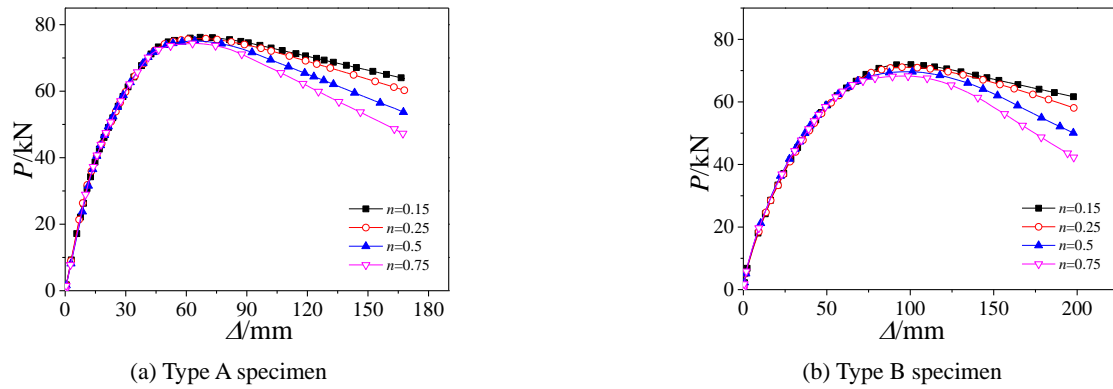


Fig. 16 The skeleton curve under different axial compression ratios

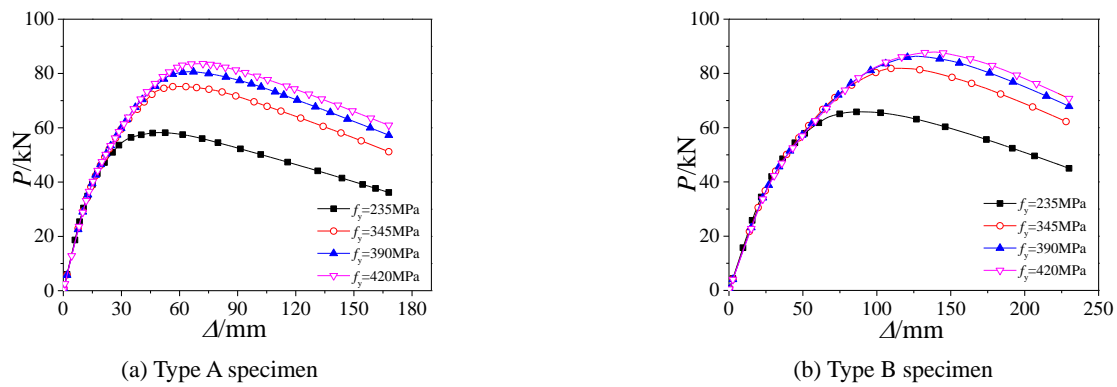


Fig. 17 The skeleton curve under different yielding strengths

The finite element calculation results are shown in Fig. 15. It can be seen from the graph that with the increase of β , the initial elastic stiffness and horizontal bearing capacity increase significantly. Within a certain range, with the increase of β , P - Δ curve of the type B specimen descends slowly after the peak point. For type A specimen, with the increase of β , the specimens both present better ductility. However, as β reaches 0.169, the P - Δ curve descends rapidly after the peak point. It can be seen that as β is too large, CFST column fails to yield in the test. In this background, the CFST column has not fully showed its better ductility and higher bearing capacity in the late loading stage (Zeghiche and Chaoui 2005). The root of RC column is destroyed seriously. Therefore, the bearing capacity decreases rapidly and the ductility is not good. As β is too small, the displacement of CFST column and RC column is not coordinated severely. The deformation of CFST column is so large as to form weak parts at the root of upper column, which makes ductility decrease. Therefore, in order to ensure good ductility of CFST-RC columns, it is necessary to control the stiffness ratio of the upper and lower bars within a reasonable range.

4.4.2 Axial compression ratio n

Experimental results show that axial compression ratio has an effect on the yielding mechanism of column. In order to further study the influence of axial compression ratio on the seismic performance of specimens, the different axial compression ratios are chosen to conduct the numerical

analysis for LJ-1 and LJ-3. The axial compression ratios are 0.15, 0.25, 0.5 and 0.75, respectively. Fig. 16 shows the skeleton curve under different axial compression ratios. It can be seen from the charts, as the axial compression ratio increases, the overall deformation of the specimen is more uncoordinated and the P - Δ effect is more and more obvious. After peak point, the skeleton curve descends rapidly with the increase of axial compression ratio.

4.4.3 Yielding strength of steel tube f_y

Fig. 17 shows the skeleton curves under different yielding strengths of steel tube. It can be seen that the strengths have few effect on the elastic lateral stiffness of specimen. With the increase of strength, the bearing capacity of specimen is improved obviously and the longitudinal rebar yields prior to the steel tube. Therefore, the concrete in the RC column is destroyed seriously, which results in that the ductility of specimen gets worse, as shown in Table 7.

4.4.4 Concrete strength $f_{cu,k}$

The skeleton curves under different concrete strengths are shown in Fig. 18. It indicates that the concrete strengths have little influence on the seismic performance of specimen. With the increase of concrete strength, the elastic stiffness and bearing capacity both are improved, while the bearing capacity decreases rapidly after the peak. The specimen shows the obvious brittle characteristic. The ductility gradually decreases as shown in Table 7.

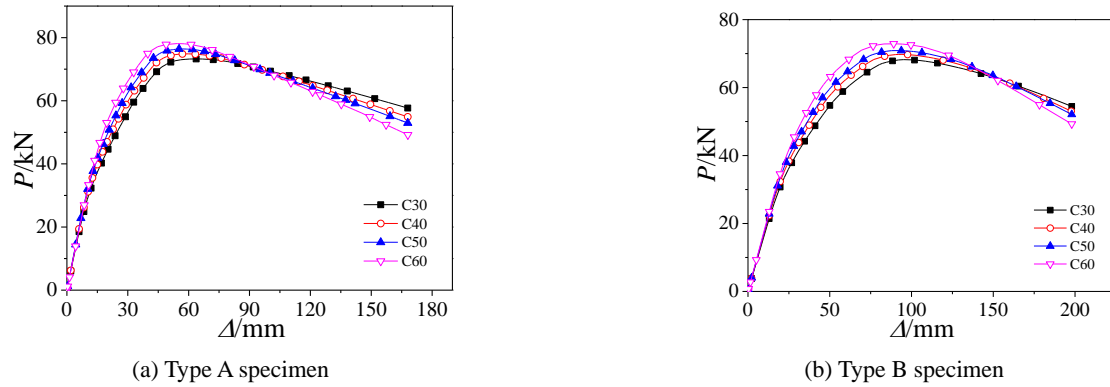


Fig. 18 The skeleton curve under different concrete strengths

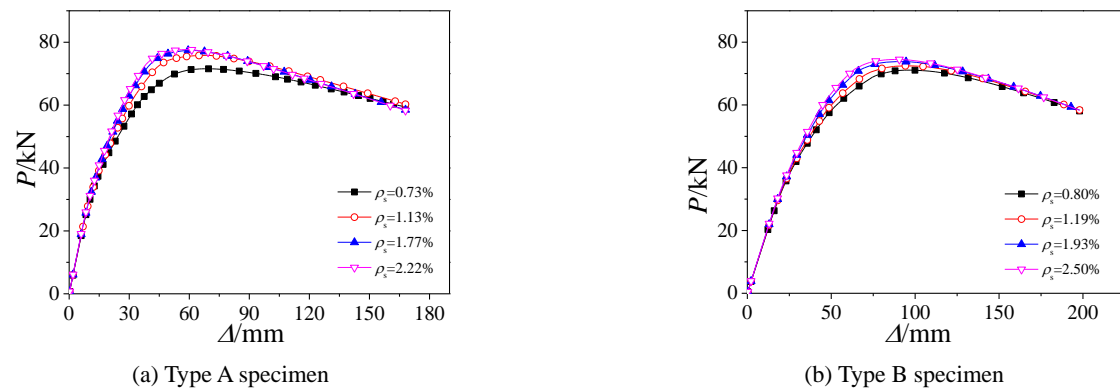


Fig. 19 The skeleton curve under different longitudinal rebar ratios

4.4.5 Longitudinal rebar ratio ρ_s

The skeleton curves under different longitudinal rebar ratios are shown in Fig. 19. The bigger ρ_s is, the bigger bearing capacity is. With the increase of longitudinal rebar ratio, the steel tube of CFST column yields followed by the longitudinal rebar in RC column, which leads to the decrease of ductility, as shown in Table 7.

5. Conclusions

In this paper, the quasi-static test is carried out for four CFST-RC mixed columns under low-cyclic revised loading. Additionally, based on the test results, the parameter analysis is conducted by ABAQUS soft. The conclusions are summarized as follows:

- The failure mode of the CFST-RC mixed column for antique buildings is mainly dominated by bending failure and accompanied by some shear failure characteristics. There are plastic hinges in the root of CFST column and RC column, and the obvious oblique shear cracks appear in the upper part of RC column.
- The axial compression ratio has an important influence on the yield mechanism of the CFST-RC mixed column. Under the larger axial compression ratio, the CFST column yields first followed by the RC column section due to the excessive lateral deformation. Conversely, the RC column first yields

followed by the CFST column.

- Under different axial compression ratios, the displacement ductility coefficients of the CFST-RC mixed columns for archaized buildings are both greater than 3, which show the specimens have good deformation capacity. The equivalent viscous damping coefficients of all the specimens are all greater than 0.2 in the failure stage, which shows the mixed columns have a higher energy dissipation capability.
- Within a reasonable range, the increase of the stiffness ratio (i_{CFST}/i_{RC}) can improve the horizontal bearing capacity and elastic stiffness, which makes the specimen have a good ductility. The stiffness ratio (i_{CFST}/i_{RC}) is too large to fully exert the ductility of CFST column. With the increase of the axial compression ratio, the horizontal bearing capacity gradually decreases as well as the ductility. The increase of parameters, including yielding strength, concrete strength and longitudinal rebar ratio, can improve the bearing capacity but decrease the ductility.

Acknowledgments

This work described in this paper was supported by the National Natural Science Foundation of China (Granted No. 51678478), CSCEC Technology Research and Development Project (Granted No. 2012-Z-16).

References

- Chacón, R., Mirambell, E. and Real, E. (2013), "Strength and ductility of concrete-filled tubular piers of integral bridges", *Eng. Struct.*, **46**(1), 234-246.
- Chitawadagi, M.V., Narasimhan, M.C. and Kulkarni, S.M. (2012), "Axial strength of circular concrete-filled steel tube columns — doe approach", *J. Constr. Steel Res.*, **66**(10), 1248-1260.
- Darvishi, E., Namdar, A., Feng, X. and Ge, Q. (2016), "Seismic resistance of timber structure-a state of the art design", *Procedia Struct. Integr.*, **2**, 2750-2756.
- Eckelman, C.A. and Haviarova, E. (2015), "Withdrawal and compression force capacity of pinned end-to-end round mortise-and-tenon wooden joints", *Wood Sci. Technol.*, **47**(3), 217-224.
- Ekmekyapar, T. and Al-Eliwi, B.J.M. (2016), "Experimental behaviour of circular concrete filled steel tube columns and design specifications", *Thin Wall Struct.*, **105**(8), 220-230.
- Ghannam, S., Jawad, Y.A. and Hunaiti, Y. (2004), "Failure of lightweight aggregate concrete-filled steel tubular columns", *Steel Compos. Struct., Int. J.*, **4**(1), 1-8.
- Gong, X. (2015), "Research on seismic performance of a reinforced concrete antique building", *J. North China Univ. Technol.*, **27**(3), 43-50.
- Hajjar, J.F. (2015), "Concrete-filled steel tube columns under earthquake loads", *Progr. Struct. Eng. Mater.*, **2**(1), 72-81.
- Han, L.H. and An, Y.F. (2014), "Performance of concrete-encased CFST stub columns under axial compression", *J. Constr. Steel Res.*, **93**(1), 62-76.
- Liu, W. (2005), "Research on mechanism of concrete-filled steel tubes subjected to local compression", Ph.D. Dissertation; Fuzhou University, Fuzhou, China.
- Ouyang, Y. and Kwan, A.K.H. (2018), "Finite element analysis of square concrete-filled steel tube (CFST) columns under axial compressive load", *Eng. Struct.*, **156**(2), 443-459.
- Patel, V.L., Uy, B., Prajwal, K.A. and Aslani, F. (2016), "Confined concrete model of circular, elliptical and octagonal CFST short columns", *Steel Compos. Struct., Int. J.*, **22**(3), 497-520.
- Portolés, J.M., Romero, M.L., Bonet, J.L. and Filippou, F.C. (2011), "Experimental study of high strength concrete-filled circular tubular columns under eccentric loading", *J. Constr. Steel Res.*, **67**(4), 623-633.
- Prabhu, G.G., Sundararaja, M.C. and Yun, Y.K. (2015), "Compressive behavior of circular CFST columns externally reinforced using CFRP composites", *Thin Wall Struct.*, **87**(2), 139-148.
- Shen, J.M., Wang, C.Z. and Jiang, J.Q. (1993), *Finite Element Analysis of Reinforced Concrete and Limit Analysis of Plate and Shell*, Tsinghua University Press, Beijing, China.
- Skalomenos, K.A., Hatzigeorgiou, G.D. and Beskos, D.E. (2015), "Modeling level selection for seismic analysis of concrete-filled steel tube/moment-resisting frames by using fragility curves", *Earthq. Eng. Struct. D.*, **44**(2), 199-220.
- Sundararaja, M.C. and Prabhu, G.G. (2013), "Flexural behaviour of CFST members strengthened using CFRP composites", *Steel Compos. Struct., Int. J.*, **15**(6), 623-643.
- Suzuki, H., Nishihara, H., Matsuzaki, Y. and Minami, K. (2000), "Structural performance of mixed member composed of steel reinforced concrete and reinforced concrete", *Proceedings of the 12th World Conf. on Earthquake Engineering*, Mexico, October.
- Wang, L. (2012), "Comparative study on structural behavior between ancient structure and antique building of a Qing-style Hall", Master Dissertation; Xi'an University of Architecture & Technology, Xi'an, China.
- Wang, J.C. and Chen, Y.K. (2006), *Application of ABAQUS in Civil Engineering*, Zhejiang University Press, Hangzhou, China.
- Wu, K., Xue, J.Y. and Zhao, H.T. (2016), "Experimental research on seismic behavior of SRC-RC transfer columns", *Steel Compos. Struct., Int. J.*, **21**(1), 157-175.
- Xue, J.Y., Wu, Z.J. and Sui, Y. (2015), "Experimental study on seismic performance of steel double-beams column exterior joints in antique style building", *J. Build. Struct.*, **36**(3), 80-89.
- Yadav, R., Chen, B., Yuan, H. and Lian, Z. (2016), "Numerical study on the seismic behavior of CFST columns", *Proceedings of the 11th Pacific Structural Steel Conference 2016*, Shanghai, October.
- Zeghiche, J. and Chaoui, K. (2005), "An experimental behavior of concrete-filled steel tubular columns", *J. Constr. Steel Res.*, **61**(1), 53-66.
- Zhao, Y. and Shao, Y.J. (2010), "Experimental study on seismic behavior of SRC-RC transfer columns with different constructional measures", *World Earthq. Eng.*, **26**(2), 119-124.

CC

Nomenclature

n	Axial compression ratio
λ	Slenderness ratio
ρ_s	Longitudinal reinforcement ratio
ρ_v	Stirrup ratio
f_y	Yielding strength of steel
f_u	Ultimate strength of steel
E_s	Elastic modulus of steel
ε_y	Yielding strain of steel
P_{cr}	Cracking load of specimen
P_y	Yield load of specimen
P_m	Peak load of specimen
P_u	Failure load of specimen
Δ_{cr}	Cracking displacement of specimen
Δ_y	Yielding displacement of specimen
Δ_m	Peak displacement of specimen
Δ_u	Failure displacement of specimen
μ	Ductility coefficient of specimen
h_e	Equivalent viscous damping coefficient
F_1	Horizontal bearing capacity under the first cycle
F_3	Horizontal bearing capacity under the third cycle
β	Stiffness ratio of the upper to lower column
$f_{cu,k}$	Standard cubic compression strength of concrete
$f_{t,r}$	Axial tension strength of concrete
$f_{c,r}$	Axial compression strength of concrete
$\varepsilon_{t,r}$	Peak strain corresponding to the $f_{t,r}$
$\varepsilon_{c,r}$	Peak strain corresponding to the $f_{c,r}$
α_t	Parameter in the decline stage of tension stress-strain curve
α_c	Parameter in the decline stage of compression stress-strain curve
$\varepsilon_{c,u}$	Compression strain corresponding to the $0.5 f_{c,r}$ in the decline stage of curve
ζ	Constraining factor of steel tube
A_s	Area of steel tube
A_c	Area of concrete section
f_{ck}	Standard axial compression strength of concrete